JOURNAL OF SPACECRAFT AND ROCKETS
Vol. 34, No. 4, July–August 1997

Three-Dimensional Hypersonic Laminar Boundary-Layer Computations for Transition Experiment Design

Roger L. Kimmel* and Mark A. Klein†
U.S. Air Force Wright Laboratory, Wright–Patterson Air Force Base, Ohio 45433-7913
and
Stephen N. Schwoerke‡
Lockheed Martin Corporation, Fort Worth, Texas 76101-0748

The stability of boundary layers on sharp-nosed cones with elliptical cross sections is assessed using linear stability theory and crossflow correlations. The objective is to identify a configuration for wind-tunnel testing that exhibits significant crossflow but also possesses a sufficient laminar region for boundary-layer stability probing. Parabolized Navier–Stokes computer codes were used to calculate the mean flow about cones with eccentricities of 1.5:1, 2.0:1, and 4.0:1 at a freestream Mach number of 7.95 and freestream unit Reynolds number of 3.3×10^6 m^{-1}. Correlations indicated that transition was possible on each configuration at the above conditions. All three configurations showed unstable, inflectional velocity profiles and boundary-layer thickening along the centerline (minor axis) due to the influx of low-momentum fluid. Crossflow separation was observed on the 2.0:1 configuration. Linear stability theory was used to calculate stationary crossflow *N* factors on all three configurations, and to calculate traveling-wave *N* factors on the 1.5:1 and 2.0:1 configurations. All three configurations showed crossflow instability, with the 4.0:1 configuration attaining the highest *N* factors. The 1.5:1 and 2.0:1 configurations were unstable to a broad spectrum of traveling waves, with the highest *N* factors attained on centerline, due to the unstable profiles there.

Nomenclature

e = eccentricity, ratio of ellipse major to minor diameters
f = frequency, kHz
H = compressibility factor,[16] dimensionless
h = enthalpy, J/kg
i = mesh index in wall-normal direction (Fig. 2)
j = mesh index in circumferential direction (Fig. 2)
k = mesh index in axial direction (Fig. 2)
L = model length, 1.016 m, or dimensionless wall cooling factor in modified crossflow Reynolds number[16]
M = Mach number
N = logarithm of the ratio of local to initial disturbance amplitudes
p = pressure, N/m^2
$\dot{q}$ = heat flux, W/m^2
R = universal crossflow parameter, $Re_{\text{cf new}} U_e / w_{\max}$, with $U_e / w_{\max}$ in percent
Re = Reynolds number
Re_{cf} = crossflow Reynolds number, $w_{\max}\delta_{10}/\nu_e$ (Ref. 16)
$Re_{\text{cf new}}$ = new crossflow Reynolds number, $HLRe_{\text{cf}}$ (Ref. 16)
St = Stanton number, $\dot{q}/\{\rho_\infty U_\infty [h(T_0) - h(T_w)]\}$
T = temperature, K
U = velocity component in direction of edge velocity and tangent to model surface, m/s
$w_{\max}$ = maximum crossflow velocity, m/s
x = axial coordinate (Fig. 2), m
y = spanwise coordinate (Fig. 2), m
z = vertical coordinate (Fig. 2), m
α = elevation angle in spherical coordinate system, deg
β = azimuthal angle in spherical coordinate system, deg
δ = boundary-layer thickness, perpendicular to model, m
δ_{10} = height above $w_{\max}$ point where crossflow is 10% of $w_{\max}$, m
η = computational radial coordinate perpendicular to model, m
θ = angular coordinate, deg (Fig. 2), or momentum thickness, m
λ = disturbance wavelength, m
ν = kinematic viscosity, m^2/s
ρ = density, kg/m^3
ψ = disturbance wave angle (normal to constant phase line) relative to edge velocity, deg

Subscripts

cf = crossflow
u = unit, per meter
w = wall conditions
∞ = freestream conditions, upstream of model bow shock
0 = stagnation conditions

Presented as Paper 96-2080 at the AIAA 27th Fluid Dynamics Conference, New Orleans, LA, June 17–20, 1996; received July 30, 1996; revision received March 14, 1997; accepted for publication March 15, 1997.

* Aerospace Engineer, WL/FIMA, 2645 Fifth Street, Suite 7. Senior Member AIAA.
† Aerospace Engineer, WL/FIMA, 2645 Fifth Street, Suite 7. Student Member AIAA.
‡ Engineering Specialist, Flight Dynamics Branch, Product Engineering Department, Tactical Aircraft Systems, P.O. Box 748.

Introduction

PREVIOUS work on hypersonic boundary-layer transition has focused on axisymmetric or two-dimensional flows. Most realistic configurations, however, include regions of three-dimensional flow. The stability and transition characteristics of three-dimensional boundary layers differ significantly from those of two-dimensional boundary layers. The most fundamental difference is that, in addition to the instability waves present in two-dimensional or axisymmetric flow, three-dimensional flows may contain crossflow instabilities. These instabilities are corotating vortices that are established when the boundary-layer edge flow direction differs sufficiently from the flow direction lower in the boundary layer.[1] This crossflow is established by a spanwise or circumferential pressure gradient, which induces a flow component perpendicular to the longitudinal axis of a body. Because the interior boundary-layer fluid possesses lower momentum than the boundary-layer edge fluid, the interior fluid is skewed more sharply than the exterior fluid. This shearing induces vorticity with a streamwise component. Vortices that increase in strength in the streamwise direction may be set

up. Under some conditions, these crossflow vortices may be the dominant disturbance leading to transition. These vortices may also convect to produce nonzero-frequency disturbances.[1,2]

Few stability computations for hypersonic, three-dimensional boundary layers exist.[3] Essentially no experimental stability data exist for these flows. For this reason, it was decided that the extensive experimental database acquired by U.S. Air Force Wright Laboratory[4] on axisymmetric hypersonic boundary-layer stability should be extended to three-dimensional configurations. An elliptic cone configuration was chosen as the candidate test geometry because of its resemblance to practical flight configurations and the geometrical advantages it offers for probe measurements. The crossflow is established by the pressure differential between the major and minor axes, which causes flow from the high-pressure major axis (leading edges) to the minor axis (top and bottom centerlines).

Computational analysis was required to select an elliptic cone geometry. The design objective was to develop a configuration that exhibits significant crossflow but presents enough laminar area to measure the stability characteristics of the boundary layer prior to transition. This paper presents the results of parabolized Navier–Stokes (PNS) and linear stability computations of the flow around three elliptic cone configurations of ellipticity $e = 1.5$, 2.0, and 4.0. The model half angle in the centerline plane was fixed at 7 deg for each configuration. The model length was 1.016 m in each case. Calculations were carried out for $M_\infty = 7.95$ and $Re_{u\infty} = 3.3 \times 10^6$ m^{-1} to match test conditions in Arnold Engineering Development Center (AEDC) Tunnel B. Transition correlations were used to identify candidate configurations for more detailed analysis. Computations were carried out for an adiabatic wall corresponding to flowfield probe measurement conditions, and for a cold wall with $T_w/T_0 = 0.42$ ($T_w = 303$ K), corresponding to measurement conditions for the mean heat transfer.

Previous Work

A large portion of the literature on three-dimensional hypersonic transition deals with cones at angle of attack. Elliptic cone experiments of any type are relatively rare. Most elliptic cone measurements have centered on pressure distributions or forces and moments. Experimental data on heat transfer, the boundary layer, and transition are extremely limited. Heat transfer data were obtained on sharp- and blunt-nosed elliptic cones at $M_\infty = 10$ and 14 (Ref. 5). The data for a sharp-nosed elliptic cone of eccentricity $e = 1.43$ at $M_\infty = 10$, replotted in Fig. 1, show the beginning of transition near the top centerline of the model. This behavior is qualitatively similar to the transition of cones at angle of attack, where the most forward point of transition is usually on the lee centerline.[6–11] Other features in the heat transfer analogous to cones at angle of attack are the increased heat transfer on the leading edge, due to the higher stagnation-line shear, and the lower heat transfer on the top centerline, due to the boundary-layer thickening caused by the influx of fluid at this location.

Crossflow instabilities in supersonic and hypersonic flow have generally been inferred experimentally from the observation of streaks in surface visualizations. Such streaks were observed in temperature-sensitive paint on the surface of a swept cylinder at $M_\infty = 10$ (Ref. 12). The wavelengths of these streaks agreed, within experimental scatter, with predictions of crossflow wavelengths. Streaks were also observed on a swept cylinder at $M_\infty = 5$ using temperature-sensitive liquid crystals.[13] The boundary-layer edge Mach numbers for these cases were supersonic, however, rather than hypersonic, on account of the model geometry. Streaks were observed on a cone at angle of attack at $M_\infty = 8$ using shear-stress-sensitive liquid crystals.[14] Numerous investigators have observed surface streaking at supersonic and subsonic Mach numbers.

Numerous correlating parameters have been proposed to predict boundary-layer transition. Correlation methods are subject to much uncertainty, especially when a correlation developed for a specific configuration is applied to a different configuration. Nevertheless, correlation methods provide a rapid means of determining the likelihood of transition. A crossflow Reynolds number Re_{cf} between 150 and 200 correlated transition data from a variety of sources and configurations for $0.3 < M_\infty < 7.4$ (Ref. 15). A greater spread in crossflow transition Reynolds number was observed for rotating cones and cones at angle of attack,[16] and a modified crossflow Reynolds number was proposed to take compressibility and wall cooling into account. Transition results from cones at angle of attack at $M_\infty = 3$ and 6 were correlated by the new crossflow Reynolds number and the crossflow velocity percentage, $100\, w_{max}/U_e$. These two parameters also correlated the $N = 9$ location on rotating cones calculated by linear stability theory. These results indicated a universal parameter R. Values of $R = 44.0$ correlated transition under quiet conditions, and $R = 33.7$ in conventional facilities, over a range of $0.02 < w_{max}/U_e < 0.08$.

PNS calculations for adiabatic wall elliptic cones of eccentricities of 2, 3, and 4 at $M_\infty = 4$ have been performed,[17] and the crossflow Reynolds number correlations were applied to these results. The parameter R for these configurations peaked near the top centerline, outside the region of validity of the above correlation. Boundary-layer velocity profiles near the top centerline were inflectional and unstable.

Results

Computational Procedures

Most of the basic state computations for the laminar boundary layer were carried out using the UPS PNS code,[18] as modified by Lockheed Martin Tactical Aircraft Systems. The code uses a central difference scheme for inviscid fluxes and a fourth-order smoothing model. Additional cold-wall cases were run using the Air Force Wright Aeronautical Laboratory PNS code.[19] All results presented in this paper, with the exception of heat transfer, are for adiabatic wall conditions. The e^{Malik} code[20] was used to calculate boundary-layer stability.

The coordinate system is shown in Fig. 2. The nose solution for the first inch of each model was obtained with a Navier–Stokes nose solution code. All three computational fluid dynamics (CFD) codes employed shock fitting to model the outer boundary. The computational grid, shown in Fig. 3, was generated by distributing points

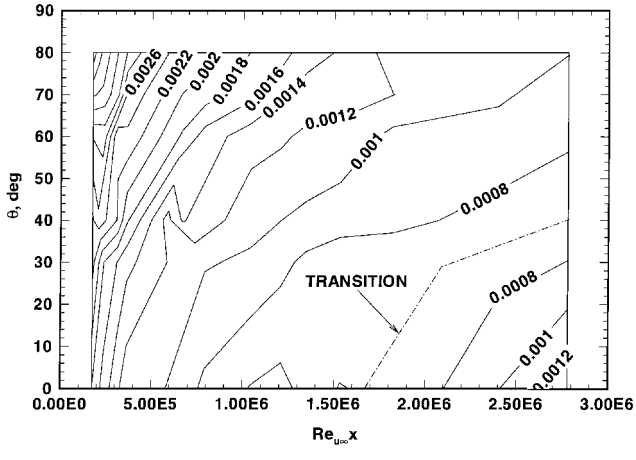

Fig. 1 Stanton number contours for $e = 1.43$ cone at $M_\infty = 10$.

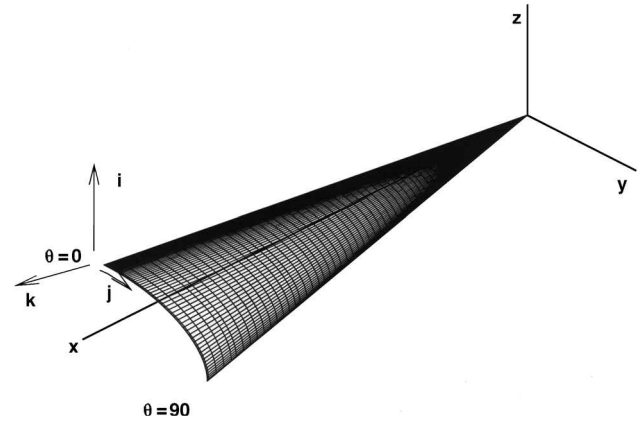

Fig. 2 Elliptic cone configuration and coordinate system.

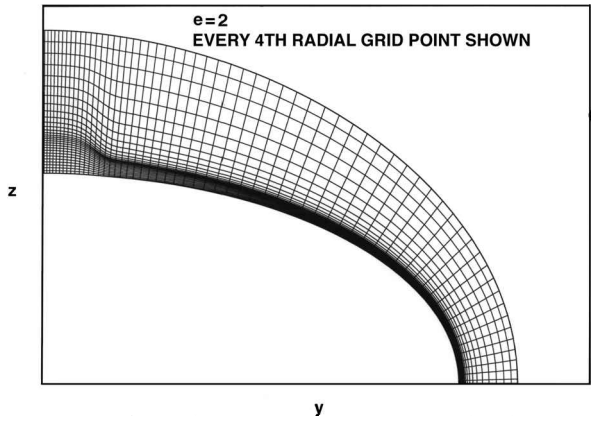

Fig. 3 PNS computational mesh on e = 2.0 elliptic cone.

along the circumference of the model at each axial cross section (x constant) and projecting the radial lines outward, normal to the body, in the $y-z$ plane. The interior points were spaced algebraically in two radial layers. The inner layer resolved the boundary layer, and the outer resolved the remainder of the flowfield. The spacing at the wall was 100% of even spacing within the inner layer. Spacing at the edge of the boundary layer was 66% of even spacing. For the outer layer, the spacing at the shock was 150% of even spacing, and the spacing at the edge of the boundary layer was set to match the spacing of the neighboring point. Each layer contained approximately half of the total radial points. The UPS code automatically adapted the grid to keep the grid layer interface at the edge of the boundary layer. Solutions were confined to one 90-deg quadrant.

Grid resolution studies were conducted on the $e = 1.5$ and 2.0 configurations. The grid dimensions $i \times j \times k$ were changed from $61 \times 51 \times 875$ to $121 \times 61 \times 875$. Only the fine-grid results are presented for these configurations. Only a $61 \times 71 \times 875$ case was run for the $e = 4.0$ configuration. Results were insensitive to grid resolution except for the high-frequency amplification rates calculated near the top centerline. At 50 kHz, for example, the amplification results were about 10% lower when the boundary-layer edge was less well resolved. Because this frequency range and region were of little consequence to the overall results, no further grid refinement was undertaken.

The effect of numerical smoothing on the basic state can be very important for a linear stability code. Too much smoothing can change the boundary-layer profile derivatives and lead to erroneous results. For this study, only fourth-order smoothing was present in the CFD solution. The smoothing constant was halved for the $e = 1.5$ fine-grid case to assess these effects. The only variations in the linear stability results were in the region near the edge of the boundary-layer buildup near the top centerline. A finer grid would be desirable here to resolve the higher flowfield gradients in this region.

Tests were conducted on the $e = 1.5$ configuration to determine the effects of linear stability approximations on stability results. Results should be qualitatively similar for the other configurations. Several parameters control the location of the outer boundary and the region the e$^{\text{Malik}}$ internal grid is clustered to. Clustering of the e$^{\text{Malik}}$ internal grid and the outer boundary location were varied, but no significant effects were observed. In the final results, the outer boundary location was set to 20 times the boundary-layer height, and the clustering parameter was set to 80% of the boundary-layer height.

The version of the e$^{\text{Malik}}$ code used did not include the coordinate-system curvature terms. The axial curvature of the coordinate system as it moves along a streamline should be small and of little consequence, because there is no destabilizing concave curvature. The transverse curvature should be more like that seen on a conical body, however. Accordingly, the conical coordinate system curvature terms were introduced into the code to get some idea of their effect. These showed amplification reductions over many regions that averaged around 10%. This calculation is not rigorously correct, but it does give some idea of the accuracy limitations of the results. A parabolized stability equation code could more easily include the curvature and nonlocal effects that the present linear stability analysis ignores.

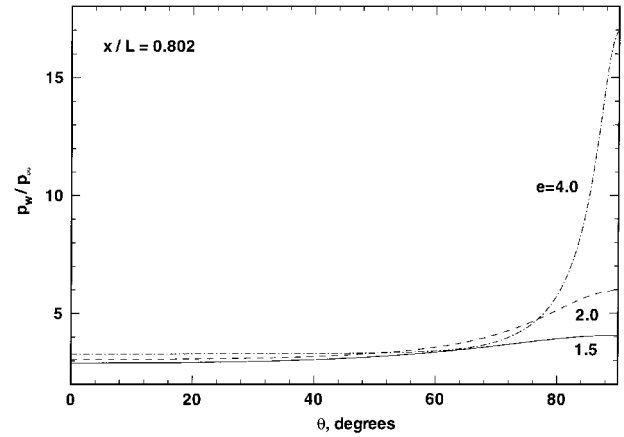

Fig. 4 Circumferential distribution of wall-to-freestream static pressure ratios.

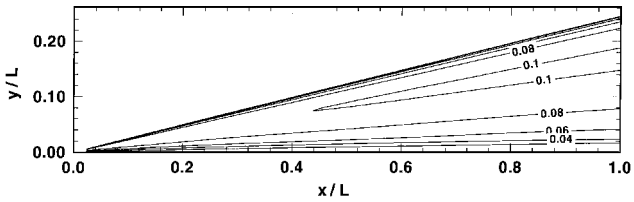

Fig. 5 Top view of crossflow velocity contours for e = 2.0 elliptic cone.

Basic State Results

The pressure distributions about the circumference of the three configurations are shown in Fig. 4. The pressure gradients between the major and minor axes establish the crossflows, and the strength of the crossflow depends on the magnitude of these gradients. Contours of $w_{\max}/U_e$ for the $e = 2.0$ configuration are shown in Fig. 5. The crossflow contour shapes for the other two configurations were similar. The maximum crossflows were 6.5, 10, and 14.5% for the $e = 1.5$, 2.0, and 4.0 configurations, respectively.

The crossflow is defined relative to the boundary-layer edge velocity, with positive crossflow defined as inboard toward the model centerline. The boundary-layer edge velocity is not, in general, parallel to a ray emanating from the model nose. At most locations the edge velocity possesses a component directed inboard due to the circumferential pressure gradient, and a component directed toward the model surface because the conical bow shock does not turn the streamlines completely parallel to the model surface. Thus a boundary-layer edge velocity direction must be defined for each radial grid line. The total-enthalpy profile was used to identify the boundary-layer edge, since it is unaffected by shock curvature and has been shown previously to correlate well with the velocity thickness for circular cones.[21] Because the Prandtl number is less than unity, the total enthalpy profile varies from less than freestream at the wall to a peak 3 to 4% above freestream within the boundary layer. The boundary-layer edge is taken as the location above the peak where the total-enthalpy is 1.005 times the stagnation enthalpy. At each circumferential station, the boundary-layer edge was identified and the edge velocity vector tangent to the surface noted. The cross product of the body normal with the edge velocity vector defined the crossflow direction for each radial grid line. The 10% maximum crossflow ratio for the $e = 2.0$ configuration compares to a peak of about 4% for the $e = 2.0$ configuration at $M_\infty = 4.0$ (Ref. 17). The increased crossflow in the present study is due to the stronger circumferential pressure gradient created by the higher Mach number.

The crossflow is illustrated by the surface (or limiting) and boundary-layer edge streamlines for the $e = 2.0$ configuration shown in Fig. 6. The edge streamlines are directed approximately along rays from the nose of the configuration, but the surface streamlines (computed from the first point off the body surface) are sharply deflected toward the centerline. The surface streamlines run parallel to but do not cross a locus near the centerline. This feature is typical of a crossflow separation. Crossflow separation was observed in a

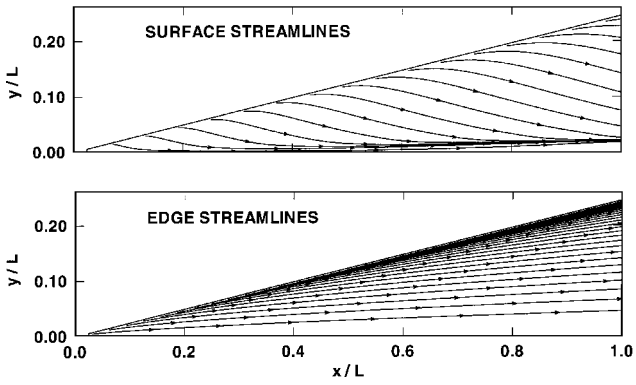

Fig. 6 Top view of surface and boundary-layer edge streamlines for the e = 2.0 configuration.

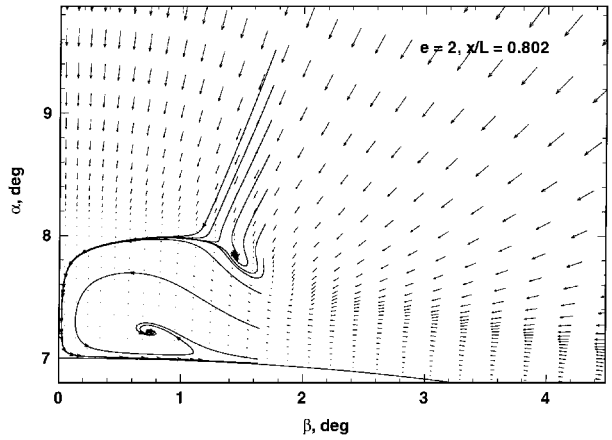

Fig. 7 Sectional streamlines in spherical coordinate system. Every fourth radial point is shown.

preliminary calculation[17] for the elliptic cone at Mach 4.0 but not in a revised calculation.[22]

To further investigate the existence of crossflow separation, sectional streamlines in the crossflow plane are plotted in Fig. 7. These velocity vectors are described in a spherical coordinate system, in which a zero-length vector represents either zero velocity magnitude or flow directed entirely along a ray from the origin at the model nose. The vectors in Fig. 7 represent flow perpendicular to rays from the origin. Although sectional streamlines may in some cases be misleading,[23] Fig. 7 provides strong evidence of crossflow separation. Crossflow separation is indicated by the liftup of sectional streamlines from the model surface near $\beta = 1.2$ deg (coincident with the surface line of convergence) and by the spiral focus located near $\beta = 0.8$ deg and $\alpha = 7.2$ deg. The vortex would be difficult to identify experimentally on account of its close proximity to the model body.

The crossflow separation or near-separation has implications for boundary-layer stability. The boundary-layer thickness in Fig. 8 illustrates the ballooning of the boundary layer near the model centerline. These results are typical of the other two configurations. This ballooning is due to the influx of low-momentum fluid from around the model circumference and increases with increasing crossflow. This results in an inflected velocity profile typical of a decelerated boundary layer, as shown in Fig. 9. This boundary layer would be expected to be unstable, a conclusion born out by the stability results described below. In contrast, velocity profiles near the leading edge and the model shoulder are full and typical of accelerated flows.

Heat transfer for $e = 2.0$ and a cold wall is shown in Fig. 10. Heat transfer is highest on the leading edge, due to the attachment line heating. The leading-edge heat transfer decays exponentially with x, as observed by Burke[5] for the elliptic cone at Mach 10. The boundary-layer buildup on the model centerline is reflected in the low heat transfer at $\theta = 0$ deg.

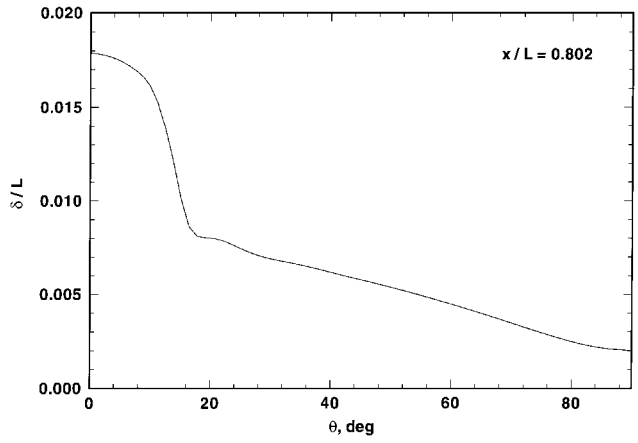

Fig. 8 Boundary-layer thickness for the e = 2.0 configuration.

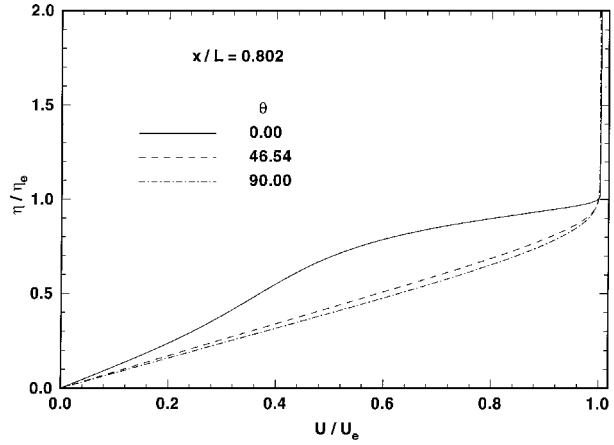

Fig. 9 U-velocity profiles for the e = 2.0 configuration.

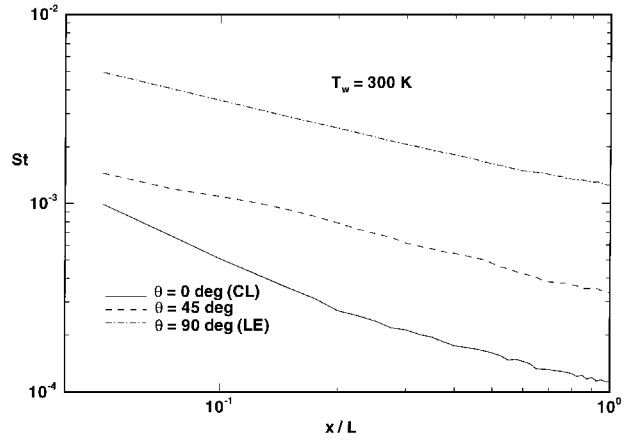

Fig. 10 Computed heat transfer for the e = 2.0 configuration, T_w / T_0 = 0.42.

Transition Correlation Results

Transition correlations based on mean flow parameters are often the only prediction tool available. Because the flow stability is related to factors such as Reynolds number and Mach number, transition correlations provide at least a gross indicator of whether a flow is near or far from transition. For these reasons, several transition criteria were examined for this study.

The conventional crossflow Reynolds number Re_{cf} is plotted in Fig. 11 for the $e = 2.0$ configuration. A typical value for crossflow transition in incompressible boundary layers is $Re_{cf} = 150$. The conventional crossflow Reynolds number over the bulk of the $e = 2.0$ configuration is about an order of magnitude larger than this. A scaling was suggested[16] to take into account the increase in boundary-layer thickness that occurs as the Mach number increases because of thermal blooming. The modified crossflow Reynolds number is

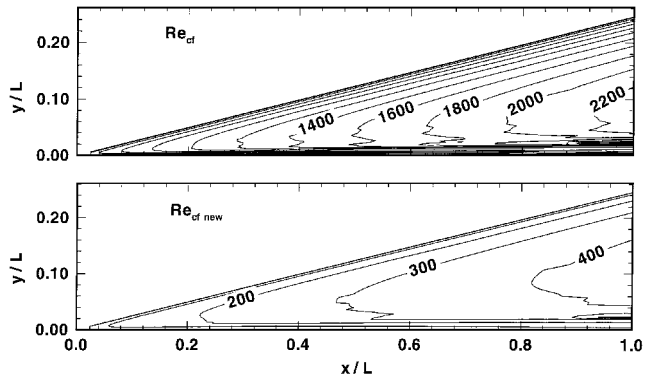

Fig. 11 Crossflow Reynolds number contours for the $e = 2.0$ configuration.

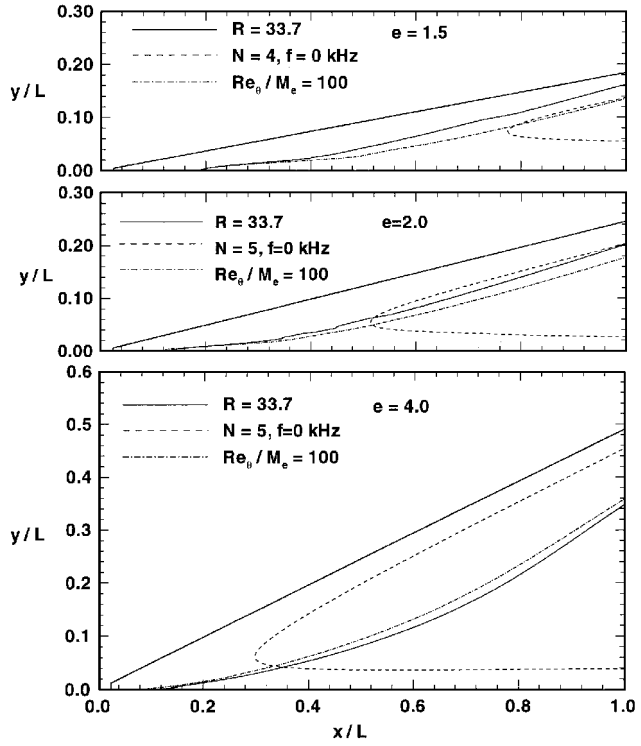

Fig. 12 Transition correlations.

defined as $HLRe_{cf}$. Here L is unity for an adiabatic wall, and H is defined as

$$\eta(\delta_{10}) \Big/ \int_0^{\eta(\delta_{10})} \left(\frac{T}{T_e}\right) \mathrm{d}\eta$$

Because T/T_e is one or greater over an adiabatic wall boundary layer, H is less than one and scales the conventional crossflow Reynolds number back into a range typical of incompressible boundary layers near transition.

The loci of $R = 33.7$ locations for the three configurations are shown in Fig. 12. Although the $R = 33.7$ contours lie, for the most part, outside the range of $0.02 < w_{\max}/U_e < 0.08$ for which the correlation was developed, they do indicate the presence of significant crossflow on each configuration. N-factor contours (discussed in the next subsection) of 4 and 5 are also shown on these plots. Contours of $R = 33.7$ do not correlate with any particular N factor.

Because velocity profiles on the model centerlines are inflectional and unstable, traveling-wave-dominated transition might occur here. To assess centerline transition, contours of the correlating parameter $Re_\theta/M_e = 100$ were plotted. In all cases, that value of Re_θ/M_e is attained on centerline at less than 20% of the body length, indicating the instability of this region.

The $Re_\theta/M_e = 100$ contours are nearly coincident with contours of $R = 33.7$. In retrospect, it might have been expected that their

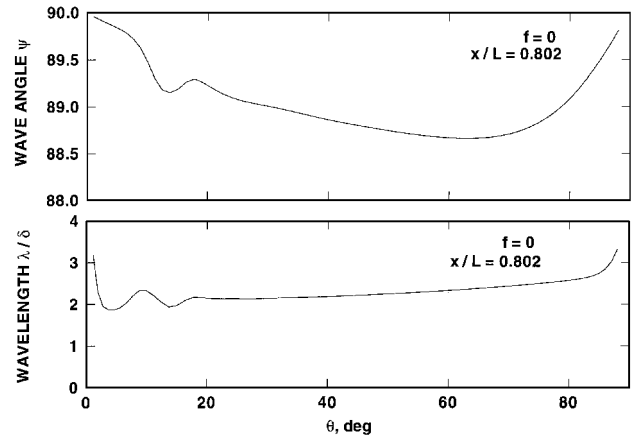

Fig. 13 Zero-frequency wave angles and wavelengths for the $e = 2.0$ configuration.

shapes would be similar. When the crossflow Reynolds number is multiplied by $U_e/w_{\max}$, the dependence on the crossflow velocity drops out,[16] leaving a Reynolds number based on δ_{10} and edge values of U and ν. The quantity H is a boundary-layer integral parameter like θ, and θ, like H, can be expressed as an integral of temperature over the boundary layer through the thermodynamic and Crocco–Busemann relations.[24] The 10% crossflow thickness δ_{10} is equal to about 90% of δ over most of the elliptic cone. It remains to be seen, however, whether the contour shapes are similar or even coincident on other configurations.

Stability Results

Zero-frequency linear stability analysis was conducted on all configurations, and multiple-frequency analysis was conducted for the $e = 1.5$ and 2.0 configurations. Zero-frequency wavelengths and wave angles are illustrated in Fig. 13. The wave angles are inclined approximately 90 deg to the boundary-layer edge velocity vectors, i.e., the vortices are approximately aligned with the boundary-layer edge streamlines. The zero-frequency wavelengths tend to be between 2 and 3 boundary-layer thicknesses, and can thus be pictured as being somewhat flattened. The $e = 2.0$ results are typical of the other two configurations.

Since the N-factor method is a correlation method, transition prediction requires that a correlating N factor be chosen. Previous computations indicated that a correlating N factor for second-mode-dominated transition for a 7-deg-half-angle sharp cone in AEDC Tunnel B is between 4 and 5 (Ref. 25). Experimental studies[10] in the NASA Langley Research Center Mach 3.5 quiet tunnel indicated that the effect of wind-tunnel noise on putatively crossflow-dominated transition was much less than the effect of noise on traveling-wave-dominated transition. This effect might be due to the fact that the wind-tunnel noise field consists primarily of convecting acoustic waves, but stationary crossflow vortices have a phase velocity of zero. The stationary disturbances might be expected to be more sensitive to zero-frequency disturbances, i.e., perturbations in the mean flow due to model roughness or wind-tunnel flow nonuniformity. These results imply that transition N factors for zero-frequency disturbances in AEDC Tunnel B might be higher than 4 or 5. Without further prior knowledge, an N factor for crossflow transition in this facility cannot be determined. Therefore, an N factor of 5 was chosen as a benchmark value indicating significant disturbance growth.

Figure 12 shows $N = 5$ contours for zero-frequency disturbances. Because the maximum N factor on the $e = 1.5$ configuration is less than 5, the $N = 4$ contour is shown instead. The N-factor contour shapes are similar to the crossflow contours in Fig. 5, indicating that for these configurations, percentage crossflow is a gross indicator of crossflow instability. The integrating effect of the N-factor procedure causes the peak N-factor contours to be shifted inboard slightly relative to the maximum crossflow contours.

Because the top centerline of the model was expected to be unstable to traveling disturbances, instabilities with frequencies of 20, 40, 60, 80, 100, 130, and 160 kHz were also calculated for the $e = 1.5$

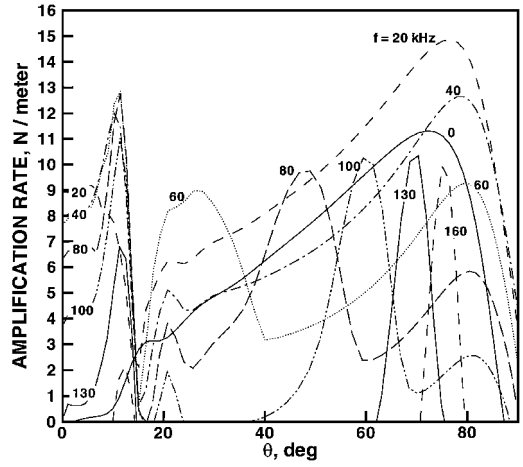

Fig. 14 Amplification rates around the circumference of the e = 2.0 configuration.

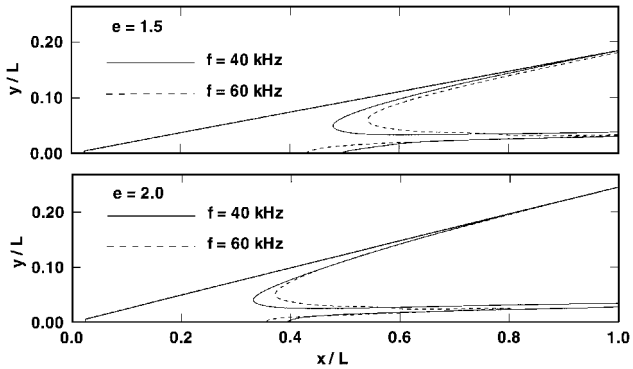

Fig. 15 N = 5 contours for 40- and 60-kHz traveling waves.

and 2.0 configurations. Figure 14 shows that a large portion of the $e = 2.0$ cone (typical) is unstable over a broad range of frequencies. This contrasts with the axisymmetric cone case,[21,25] which shows a well-defined first- and second-mode merged instability region with damped disturbances outside of this range. The three-dimensional instability behavior is reminiscent of the leeward centerline of a 7-deg sharp cone at 2-deg angle of attack, which exhibited broadband instability.[9]

N factors were calculated for each of the above frequencies, integrating along both the streamline and group velocity directions. The differences between streamline and group velocity integration were negligible. Contours of 40 and 60 kHz, which attained $N = 5$ earliest, are shown in Fig. 15. These contours are double-lobed. The outboard lobe is associated with the region of maximum crossflow, and the inboard lobe is associated with the unstable profile near the model centerline. These results are analogous to linear stability computations for a cone at angle of attack in supersonic flow,[26] which also showed a mix of stationary and traveling disturbances, with high amplification on the leeward centerline due to inflected velocity profiles there.

Conclusions

The $e = 4.0$ configuration was eliminated as a test configuration because an N factor of 5 for zero-frequency disturbances occurred at about 30% of the body length, indicating possible early transition and leaving little room for probing the boundary layer prior to transition. Also, the boundary-layer buildup on the model centerline was larger than in the other two configurations, indicating a possible early transition on the centerline, which might contaminate the off-centerline transition process.

The $e = 1.5$ and 2.0 configurations were unstable to a broad band of traveling disturbances. These configurations displayed traveling-wave N factors of 5 early on the model centerline. In the crossflow region, traveling-wave N factors of 5 occurred at 40–50% of the model length. Given that N factors of stationary and traveling waves are roughly equivalent, the transition process is likely to be mixed-mode, with contributions from both traveling and crossflow instabilities. It may be necessary in the experiment to place roughness on the model surface to force standing-wave dominance. The $e = 2.0$ configuration was chosen for fabrication because it showed higher crossflow N factors than the $e = 1.5$ configuration.

The buildup and instability of the centerline boundary layer is a problem that must be dealt with in any flight configuration that exhibits inboard-directed crossflow. It is possible that the body might be contoured in some way to alleviate this buildup and stabilize the boundary layer. Future research should also consider the blunt-nose elliptic cone configuration. This configuration offers a more complex but more realistic flight geometry. Also, bluntness can remove second-mode instabilities on axisymmetric cones. If traveling waves could be sufficiently stabilized, the crossflow instability might be isolated.

References

[1]Reed, H. L., and Saric, W. S., "Stability of Three-Dimensional Boundary Layers," *Annual Review of Fluid Mechanics*, Vol. 21, 1989, pp. 235–284.

[2]Cattafesta, L. N., III, Iyer, V., Masad, J. A., King, R. A., and Dagenhart, J. R., "Three-Dimensional Boundary-Layer Transition on a Swept Wing at Mach 3.5," *AIAA Journal*, Vol. 33, No. 11, 1995, pp. 2032–2037.

[3]Herbert, T., Stuckert, G. K., and Lin, N., "Method for Transition Prediction in High-Speed Boundary Layers," U.S. Air Force Wright Lab., TR WL-TR-93-3097, Wright–Patterson AFB, OH, Sept. 1993.

[4]Stetson, K. F., and Kimmel, R. L., "On Hypersonic Boundary-Layer Stability," AIAA Paper 92-0737, Jan. 1992.

[5]Burke, G. L., "Heat Transfer and Pressure Distributions About Sharp and Blunt Elliptic Cones at Angles of Attack and High Mach Numbers," U.S. Air Force Flight Dynamics Lab., TR AFFDL-TR-64-172, Wright–Patterson AFB, OH, May 1965.

[6]McCauley, W. D., Saydah, A. R., and Bueche, J. F., "Effect of Spherical Roughness on Hypersonic Boundary-Layer Transition," *AIAA Journal*, Vol. 4, No. 12, 1966, pp. 2142–2148.

[7]DiCristina, V., "Three-Dimensional Boundary Layer Transition on a Sharp 8° Cone at Mach 10," *AIAA Journal*, Vol. 8, No. 5, 1970, pp. 852–856.

[8]Stetson, K. F., "Mach 6 Experiments of Transition on a Cone at Angle of Attack," *Journal of Spacecraft and Rockets*, Vol. 19, No. 5, 1982, pp. 397–403.

[9]Stetson, K. F., Thompson, E. R., Donaldson, J. C., and Siler, L. G., "Laminar Boundary Layer Stability Experiments on a Cone at Mach 8, Part 3: Sharp Cone at Angle of Attack," AIAA Paper 85-0492, Jan. 1985.

[10]King, R. A., "Mach 3.5 Boundary-Layer Transition on a Cone at Angle of Attack," AIAA Paper 91-1804, June 1991.

[11]Holden, M., Bower, D., and Chadwick, K., "Measurements of Boundary Layer Transition on Cones at Angle of Attack for Mach Numbers from 11 to 13," AIAA Paper 95-2294, June 1995.

[12]Arnal, D., Vignau, F., and Laburthe, F., "Recent Supersonic Transition Studies with Emphasis on the Swept Cylinder Case," *Boundary Layer Transition and Control Proceedings* (Peterhouse College, Cambridge, England, UK), Royal Aeronautical Society, London, 1991, pp. 3.1–3.14.

[13]Murakami, A., Stanewsky, E., and Krogman, P., "Boundary Layer Transition on Swept Cylinders at Hypersonic Speeds," *AIAA Journal*, Vol. 34, No. 4, 1996, pp. 649–654.

[14]Oberkampf, W. L., Aeschliman, D. P., Tate, R. E., and Henfling, J. F., "Experimental Aerodynamics Research on a Hypersonic Vehicle," Sandia National Labs., Rept. SAND92-1411, Albuquerque, NM, April 1993.

[15]Pate, S. R., "Dominance of Radiated Aerodynamic Noise on Boundary-Layer Transition in Supersonic–Hypersonic Wind Tunnels, Theory and Application," Arnold Engineering Development Center, TR AEDC-TR-77-107, Arnold AFB, TN, March 1978, p. 49.

[16]Reed, H. L., and Haynes, T. S., "Transition Correlations in Three-Dimensional Boundary Layers," *AIAA Journal*, Vol. 32, No. 5, 1994, pp. 923–929.

[17]Lyttle, I. J., and Reed, H. L., "Use of Transition Correlations for Three-Dimensional Boundary Layers Within Hypersonic Flows," AIAA Paper 95-2293, June 1995.

[18]Lawrence, S. L., Tannehill, J. C., and Chaussee, D. S., "An Upwind Algorithm for the Parabolized Navier–Stokes Equations," AIAA Paper 86-1117, May 1986.

[19]Stalnaker, J. F., Nicholson, L. A., Hanline, D. S., and McGraw, E. H., "Improvements to the AFWAL Parabolized Navier–Stokes Code Formulation," U.S. Air Force Wright Aeronautical Labs., TR AFWAL-TR-86-3076, Wright–Patterson AFB, OH, Sept. 1986.

[20]Malik, M. R., "e^{Malik}: a New Spatial Stability Analysis Program for Transition Prediction Using the e^N Method," High Technology Corp., Rept. HTC-8902, Hampton, VA, March 1989.

[21]Stetson, K. F., Thompson, E. R., Donaldson, J. C., and Siler, L. G., "Laminar Boundary Layer Stability Experiments on a Cone at Mach 8, Part 1: Sharp Cone," AIAA Paper 83-1761, July 1983.

[22]Lyttle, I. J., and Reed, H. L., "Use of Transition Correlations for Three-Dimensional Boundary Layers Within Hypersonic, Viscous Flows," *Proceedings of the Second Symposium on Transitional and Turbulent Compressible Flows*, FED Vol. 224, Fluids Engineering Div., American Society of Mechanical Engineers, New York, 1995, pp. 87–94.

[23]Perry, A. E., and Chong, M. S., "Topology of Flow Patterns in Vortex Motions and Turbulence," *Eddy Structure Identification in Free Turbulent Shear Flows* (Proceedings of the 1992 International Union of Theoretical and Applied Mechanics Symposium, Poitiers, France), edited by J.-P. Bonnet and M. Glauser, Kluwer Academic, Hingham, MA, 1993.

[24]Schlichting, H., *Boundary-Layer Theory*, 7th ed., McGraw–Hill, New York, 1979, p. 330.

[25]Mack, L. M., "Boundary-Layer Stability Analysis for Sharp Cones at Zero Angle-of-Attack," U.S. Air Force Wright Aeronautical Labs., TR AFWAL-TR-86-3022, Wright–Patterson AFB, OH, Aug. 1986.

[26]Malik, M. R., and Balakumar, P., "Instability and Transition in Three-Dimensional Supersonic Boundary Layers," AIAA Paper 92-5049, Dec. 1992.

B. A. Bhutta
Associate Editor